Mid-infrared pulse generation using multi-plate white-light generation and optical parametric amplification in LiGaS₂ crystals

Kotaro Nakagawa[1], Nobuhisa Ishii[2*], Yoshihiko Kanemitsu[1*], and Hideki Hirori[1*]

[1]*Institute for Chemical Research, Kyoto University, Uji, Kyoto 611-0011, Japan*

[2]*Kansai Photon Science Institute, National Institutes for Quantum Science and Technology (QST), Kizugawa, Kyoto, 619-0215, Japan*

E-mail: ishii.nobuhisa@qst.go.jp, kanemitu@scl.kyoto-u.ac.jp, hirori@scl.kyoto-u.ac.jp

We demonstrate an intense mid-infrared pulse generation with a pulse energy of up to 6.2 μJ and a tunable wavelength range of 5.3–7.4 μm. This light source is based on white-light generation by multi-plate pulse compression of the output of a commercial Yb:KGW laser pulse followed by intra-pulse difference frequency generation (DFG) and optical parametric amplification in LiGaS₂ crystals. Due to the use of intra-pulse DFG, we were able to generate carrier-envelope phase (CEP)-stable mid-infrared optical pulse with a CEP standard deviation of 114 mrad, corresponding to a timing fluctuation of 360 attoseconds during the 5-hour-long measurement.

In the last two decades, the development in the field of intense ultrashort pulse lasers together with mid-infrared (MIR) light generation using optical parametric amplifiers (OPAs) has enabled the observation of extreme nonlinear optical phenomena such as high-order harmonic generation (HHG) in bulk crystals.[1–3] In particular, efficient HHG can be induced by ultrashort MIR pulses due to their relatively long wavelength,[4–8] which results in a larger ponderomotive (kinetic) energy of the electrons compared to that achieved with visible or near-infrared laser pulses. Furthermore, the motion of the electrons responsible for the HHG signal is coherent with the applied laser field. Thus, in investigations of the HHG mechanism, it is highly desirable to use a light source with a stable carrier-envelope phase (CEP).[9,10] The optical parametric amplification of a weak MIR pulse generated by intra-pulse difference frequency generation (DFG) allows us to obtain high-intensity CEP-stabilized MIR pulses, because the random phase offsets of the two rays with different wavelengths used for DFG cancel each other. Regarding the required generation of seed pulse for DFG, the high-intensity continuum generation in solids using multi-plate pulse compression has advantages in terms of system size and/or handling, compared to the characteristics of continuum generation in gases and hollow-core fibers.[11–18] Additionally, to investigate HHG in various different materials, we require a CEP-stable MIR light source that can be tuned over a wide wavelength range to efficiently induce the corresponding transitions.[19–22] So far, CEP-stable OPA light sources with white-light generation using multi-plate pulse compression have been developed for wavelengths of about 3 μm and 10 μm using $KTiOAsO_4$ (KTA) and GaSe crystals, respectively, but a light source for the 5–7 μm region with the same scheme has not yet been reported.[23–25]

In this work, we report the generation of a high-intensity MIR optical pulse with a stable CEP and a tunable wavelength range of 5.3–7.4 μm using a commercial Yb:KGW laser source. This system uses multi-plate pulse compression to generate high-intensity seed pulses, and intra-pulse DFG in a $LiGaS_2$ (LGS) crystal to generate the MIR pulses. By using a two-stage OPA, pulse energies of up to 6.2 μJ were achieved. To characterize the CEP stability, the electric-field waveform of the MIR pulses was measured by electro-optic (EO) sampling.

The experimental setup is shown in Fig. 1(a). This setup also includes the optical components for the EO sampling. A commercial Yb:KGW laser (Pharos PH2SP, Light

Conversion; pulse duration 190 fs, and center wavelength 1033 nm) was used as the light source. The laser repetition rate can be controlled by the pulse picker of the Yb:KGW laser system. By using a beam splitter (BS), the output beam of the Yb:KGW laser was first divided into the beam for the pump pulse (reflected beam) and the beam for the seed and the EO-sampling gate pulses (transmitted beam) with pulse energies of 0.9 mJ and 0.2 mJ, respectively [Fig. 1(a); BS1]. By using a second BS (BS2), the beam for the pump pulse was further divided to pump the two LGS crystals of the two-stage OPA.

To obtain the seed pulse for MIR generation and the gate pulse for EO sampling, we spectrally broadened the fundamental pulse by using a two-step multi-plate pulse compression scheme. Twelve fused-silica plates were arranged in pairs to minimize aberration and dispersion, and additionally we used a chirp mirror (CM1) for dispersion compensation and pulse compression. The two groups of plates before and after the CM1 are denoted by MP1 and MP2, respectively. The white-light pulse energy after MP2 was 0.14 mJ. Then, the spectrally broadened beam was divided into the beams for MIR generation and EO sampling by a third BS (BS3). After BS3, chirp compensation was performed for each beam using chirp mirrors (CMs) to maximize the MIR intensity in the seed pulse and to improve the temporal resolution of the EO measurements. The white-light spectrum after the CM for the gate pulse [Fig. 1(a); CM3] was measured by a spectrometer (Spectra Pro, Teledyne Princeton Instruments) attached to a charge-coupled device camera (PIXIS, Teledyne Princeton Instruments) and a spectrometer (Shamrock 163, Andor Technology Ltd.) attached to an InGaAs camera (iDus 490 Series, Andor Technology Ltd.). For the characterization of the gate pulse, we performed second-harmonic generation frequency-resolved optical gating (SHG-FROG) measurements using a beta barium borate crystal with a thickness of 10 μm [the measured and retrieved two-dimensional (2D) maps are shown in Fig. 1(b)]. We confirmed that the gate-pulse duration is 14 fs behind the CM3 [Fig. 1(c)].

The seed pulse was used to generate the MIR pulse by DFG, and then the MIR pulse was amplified by two OPAs (OPA1 and OPA2). Here, the conditions for energy conservation and phase matching are as follows:[26]

$$\omega_p = \omega_s + \omega_i \ , \tag{1}$$

$$\boldsymbol{k}_p = \boldsymbol{k}_s + \boldsymbol{k}_i \ . \tag{2}$$

Here, ω_p, ω_s and ω_i are the angular frequencies for the pump, signal, and idler pulses, respectively, and $\boldsymbol{k}_p$, $\boldsymbol{k}_s$ and $\boldsymbol{k}_i$ are the corresponding wave vectors. We chose an orientation of the crystal axis and a polarization direction of the incident pulses to satisfy Eqs. (1) and (2). We also use the definition

$$\Delta \boldsymbol{k} = \boldsymbol{k}_p - \boldsymbol{k}_s - \boldsymbol{k}_i \ . \tag{3}$$

Figure 2 shows the phase-matching function $|sinc(\Delta k L/2)|$ derived from equations 1 and 2 for the LGS crystals as functions of the phase-matching angle and the MIR wavelength. L is the interaction length of the signal, pump, and idler pulses. The refractive indices used in these calculations were taken from Refs. [27] and [28]. From these figures, we determined the following conditions for DFG:

$$6000.0(e) + 1126.7(o) = 948.6(e) \ , \tag{4}$$
$$\theta = 90.0 \ \text{deg} \ , \tag{5}$$
$$\phi = 39.9 \ \text{deg} \ , \tag{6}$$

and the following conditions for optical parametric amplification:

$$6000.0(e) + 1243.5(o) = 1030.0(e) \ , \tag{7}$$
$$\theta = 90.0 \ \text{deg} \ , \tag{8}$$
$$\phi = 39.2 \ \text{deg} \ . \tag{9}$$

Here, (e) indicates the extraordinary ray, (o) indicates the ordinary ray, and θ and ϕ are the angles of the crystal relative to the input pulse. Hence, LGS crystals with $\theta = 90°$ and $\phi = 40°$ were prepared, and the wavelength of the MIR pulse was changed by rotating the crystals in the XY plane.

In DFG, MIR pulse is generated by using two rays (with different wavelengths) in the spectrally broadened pulse. As shown in Fig. 1(a), a 1-mm-thick LGS crystal was used for DFG, and the seed pulse was focused on the crystal by a concave mirror. A germanium (Ge)

window with a thickness of 3 mm was placed behind the DFG crystal to transmit only the MIR pulse to the two-stage OPA. We used 2-mm-thick LGS crystals as OPA crystals. In each OPA, the MIR pulse was focused by a CaF_2 lens on the non-collinearly pumped OPA crystal. The pump pulse for OPA1 and OPA2 had pulse energies of 0.09 mJ and 0.81 mJ, respectively, as shown in Fig. 1(a). The beam diameters of the pump pulse were down-collimated by convex-concave lens pairs.

Figure 3 shows the generated MIR spectra (the upper and lower panels show the spectra without and with amplification in the OPAs, respectively). These spectra were measured by a Fourier-transform spectrometer (FTIR, Fastlite) as indicated in Fig. 1(a). As indicated in the lower panel of Fig. 3, the center wavelength of this light source can be tuned over the range of 5.3–7.4 μm. In this range, the maximum MIR pulse energy of 6.2 μJ with 2 mm × 2 LGS crystals for two OPAs was obtained at 5.8 μm, which corresponds to a quantum efficiency of about 3.6 % (6.2 μJ/970 μJ×5800 nm/1033 nm). We can compare this value with values reported in previous work on LGS-based OPA systems, where the total input energy was 187 μJ (white-light generation, NOPA, DFG) and the output MIR energy was 0.22 μJ.[29] Thus, the quantum efficiency at 10 μm is estimated to be 1.1%, which is about three times smaller than the value achieved in our system. The electric field strength was 25 MV/cm in vacuum when the MIR pulse was focused by a parabolic mirror (PM) with a focal length of 50 mm (spot diameter: 97 μm). Regarding the stability of the MIR pulse intensity, we obtained an rms error of 0.98% for a 25-minute-long measurement with an integration time of 5 s.

Compared to other systems,[29,30] the MIR output of our two-stage OPA has a relatively short wavelength, which can also be understood from the MIR intensity after DFG (Fig. 3; upper panel): the intensity decreases for center wavelengths larger than 6 μm, which is the same behavior as that shown by the red dots in the lower panel of Fig. 3. A DFG intensity reduction for larger center wavelengths can in principle be due to the chirp or the polarization of the white light. However, as the MIR wavelength becomes longer, the wavelengths of the two rays in the white-light beam that are used in DFG come closer together. Thus, the effect of the chirp is expected to decrease, which is not consistent with the experimental results. On the other hand, the effect of polarization is opposite to that of the chirp. As mentioned in the explanation of the phase-matching condition, the polarization directions of the two rays

in the white-light beam that are used in DFG need to be orthogonal. When longer MIR wavelengths are generated, the wavelengths of the two rays come closer together, and thus a stronger reduction of the DFG efficiency is expected as the polarization directions are approximately parallel. Note that the DFG efficiency is smaller in the case that the broadband pump pulse for DFG is linearly polarized and tilted by 45 degrees. We think that this is because the pump-pulse component that can be used for DFG in the tilted case is smaller than the pump-pulse component in the case of no tilting.

Finally, we determined the CEP stability of the MIR pulses of this system by EO sampling. As shown in Fig. 1(a), we detected the gate pulse by a balanced photodiode (BPD), and we inserted a quarter-wave plate (QWP) and a polarizing beam splitter (PBS) between the EO crystal and the detector. The EO crystal used for detection was a 30-μm-thick GaSe crystal cleaved perpendicular to the c-axis. To detect MIR pulse at 6 μm, it is necessary to prepare a gate pulse with a temporal width which is shorter than a single cycle of the MIR pulse (20 fs). As shown in Fig. 1(c), we obtained a 14-fs gate pulse by dispersion compensation with CMs after the spectral broadening of the fundamental pulse by multi-plate pulse compression. The obtained time-domain waveform of the 6-μm optical pulse is shown in Fig. 4(a). The estimated pulse width of the MIR pulse is 100 fs. The Fourier transform of the time-domain waveform is provided in Fig. 4(b), which shows a peak at 6 μm. The result of repeating such EO measurements over 20 minutes is shown in Fig. 4(c). The CEP of the MIR pulse is also shown on the right-hand side. It can be seen that the CEP is almost constant. The CEP stability over a long period of 5 hours was 114 mrad (0.36 fs) as shown in Fig. 4(d). This standard deviation was obtained from 21 average waveforms (each average waveform is derived from 10 waveforms, and the 375 points of each waveform were measured within 10 s), and was evaluated based on Fourier analysis [31]. Note that the observed CEP fluctuation includes the timing jitter between the gate pulse and that of the MIR pulse.

To conclude, we have specified the phase-matching conditions for MIR pulse generation using a Yb:KGW laser and LGS crystals, and have demonstrated an actual MIR light source with a tunable wavelength range of 5.3–7.4 μm and a maximum pulse energy of 6.2 μJ. The direct observation of the MIR electric-field waveform by EO sampling showed that the CEP was stable with a standard deviation of 114 mrad, corresponding to a timing fluctuation of

360 attoseconds during the 5-hour-long measurement. This CEP-stable light source may be used, for example, as an excitation light source in investigations on HHG in the 5–7 μm regime to achieve a deeper understanding of ultrafast electron dynamics in the nonperturbative excitation regime.

Acknowledgments

References

1) A. H. Chin, O. G. Calderón, and J. Kono, Phys. Rev. Lett. **86**, 3292 (2001).

2) S. Ghimire, A. D. DiChiara, E. Sistrunk, P. Agostini, L. F. DiMauro, and D. A. Reis, Nat. Phys. **7**, 138 (2011).

3) O. Schubert, M. Hohenleutner, F. Langer, B. Urbanek, C. Lange, U. Huttner, D. Golde, T. Meier, M. Kira, S. W. Koch, and R. Huber, Nat. Photon. **8**, 119 (2014).

4) R. A. Kaindl, M. Wurm, K. Reimann, P. Hamm, A. M. Weiner, and M. Woerner, J. Opt. Soc. Am. B **17**, 2086 (2000).

5) T. Zentgraf, R. Huber, N. C. Nielsen, D. S. Chemla, and R. A. Kaindl, Opt. Express **15**, 5775 (2007).

6) D. Brida, M. Marangoni, C. Manzoni, S. De Silvestri, and G. Cerullo, Opt. Lett. **33**, 2901 (2008).

7) A. Sell, A. Leitenstorfer, and R. Huber, Opt. Lett. **33**, 2767 (2008).

8) N. Ishii, K. Kaneshima, K. Kitano, T. Kanai, S. Watanabe, and J. Itatani, Opt. Lett. **37**, 4182 (2012).

9) M. Hohenleutner, F. Langer, O. Schubert, M. Knorr, U. Huttner, S. W. Koch, M. Kira, and R. Huber, Nature **523**, 572 (2015).

10) Y. Sanari, T. Otobe, Y. Kanemitsu, and H. Hirori, Nat. Commun. **11**, 3069 (2020).

11) C.-H. Lu, Y.-J. Tsou, H.-Y. Chen, B.-H. Chen, Y.-C. Cheng, S.-D. Yang, M.-C. Chen, C.-C. Hsu, and A. H. Kung, Optica **1**, 400 (2014).

12) P. He, Y. Liu, K. Zhao, H. Teng, X. He, P. Huang, H. Huang, S. Zhong, Y. Jiang, S. Fang, X. Hou, and Z. Wei, Opt. Lett. **42**, 474 (2017).

13) J. E. Beetar, S. Gholam-Mirzaei, and M. Chini, Appl. Phys. Lett. **112**, 051102 (2018).

14) C. Grebing, M. Müller, J. Buldt, H. Stark, and J. Limpert, Opt. Lett. **45**, 6250 (2020).

15) Q. Bournet, F. Guichard, M. Natile, Y. Zaouter, M. Joffre, A. Bonvalet, I. Pupeza, C. Hofer, F. Druon, M. Hanna, and P. Georges, Opt. Lett. **47**, 261 (2022).

16) Q. Bournet, M. Jonusas, A. Zheng, F. Guichard, M. Natile, Y. Zaouter, M. Joffre, A. Bonvalet, F. Druon, M. Hanna, and P. Georges, Opt. Lett. **47**, 4885 (2022).

17) T. Nagy, S. Hädrich, P. Simon, A. Blumenstein, N. Walther, R. Klas, J. Buldt, H. Stark, S. Breitkopf, P. Jójárt, I. Seres, Z. Várallyay, T. Eidam, and J. Limpert, Optica **6**, 1423 (2019).

18) L. Arias, A. Longa, G. Jargot, A. Pomerleau, P. Lassonde, G. Fan, R. Safaei, P. B. Corkum,

F. Boschini, H. Ibrahim, and F. Légaré, Opt. Lett. **47**, 3612 (2022).

19) Y. Sanari, H. Hirori, T. Aharen, H. Tahara, Y. Shinohara, K. L. Ishikawa, T. Otobe, P. Xia, N. Ishii, J. Itatani, S. A. Sato, and Y. Kanemitsu, Phys. Rev. B **102**, 041125(R) (2020).

20) K. Nakagawa, H. Hirori, Y. Sanari, F. Sekiguchi, R. Sato, M. Saruyama, T. Teranishi, and Y. Kanemitsu, Phys. Rev. Mater. **5**, 016001 (2021).

21) K. Nakagawa, H. Hirori, S. A. Sato, H. Tahara, F. Sekiguchi, G. Yumoto, M. Saruyama, R. Sato, T. Teranishi, and Y. Kanemitsu, Nat. Phys. **18**, 874 (2022).

22) F. Sekiguchi, G. Yumoto, H. Hirori, and Y. Kanemitsu, Phys. Rev. B **106**, L241201 (2022).

23) N. Ishii, P. Xia, T. Kanai, and J. Itatani, Opt. Express **27**, 11447 (2019).

24) Y. Sanari, F. Sekiguchi, K. Nakagawa, N. Ishii, Y. Kanemitsu, and H. Hirori, Opt. Lett. **46**, 5280 (2021).

25) N. Kanda, N. Ishii, J. Itatani, and R. Matsunaga, Opt. Express **29**, 3479 (2021).

26) R. W. Boyd, *Nonlinear Optics* (Academic Press, 2008), 3rd ed.

27) S. B. Penwell, L. Whaley-Mayda, and A. Tokmakoff, Opt. Lett. **43**, 1363 (2018).

28) S. N. Smetanin, M. Jelínek, V. Kubeček, A. F. Kurus, V. N. Vedenyapin, S. I. Lobanov, and L. I. Isaenko, Opt. Mater. Express **10**, 1881 (2020).

29) B.-H. Chen, E. Wittmann, Y. Morimoto, P. Baum, and E. Riedle, Opt. Express **27**, 21306 (2019).

30) M. Knorr, J. Raab, M. Tauer, P. Merkl, D. Peller, E. Wittmann, E. Riedle, C. Lange, and R. Huber, Opt. Lett. **42**, 4367 (2017).

31) L. Lepetit, G. Chériaux, and M. Joffre, J. Opt. Soc. Am. B **12**, 2467 (1995).

Figure Captions

Fig. 1. (a) Experimental setup. (b) Measured (left) and retrieved (right) SHG-FROG traces of the gate pulse. (c) Time-domain waveform of the retrieved gate pulse (left) and the spectrum of the pulse after CM3 (right). Here, CM1: Edmund Optics (highly-dispersive ultrafast mirror), GDD=−500 fs^2 @ 1000–1060 nm; CM2: custom made, GDD ~ −50 fs^2 @ 725 nm–1325 nm, and CM3: Edmund Optics (ultra-broadband complementary chirped mirror), GDD=−60 fs^2 @ 650–1350 nm.

Fig. 2. (a) Phase-matching conditions in the LGS crystals for DFG (upper panel) and (b) optical parametric amplification (lower panel). The phase-matching function |sinc($\Delta kL/2$)| is shown as functions of the phase-matching (PM) angle and the MIR wavelength.

Fig. 3. (a) MIR spectra before (upper panel) and (b) after the two-stage OPA (lower panel). The red dots in the lower panel show the pulse energy. The inset shows the spatial beam profile of the MIR beam at 6 μm after the LGS (OPA2).

Fig. 4. (a) The time-domain waveform of the MIR pulse after the two-stage OPA. (b) The Fourier transform of (a). (c) 2D map of 401 time-domain waveforms measured within 20 minutes (left) and the corresponding CEPs (right). (d) 2D map of 21 average time-domain waveforms measured within 5 hours (left) and their CEPs (right).
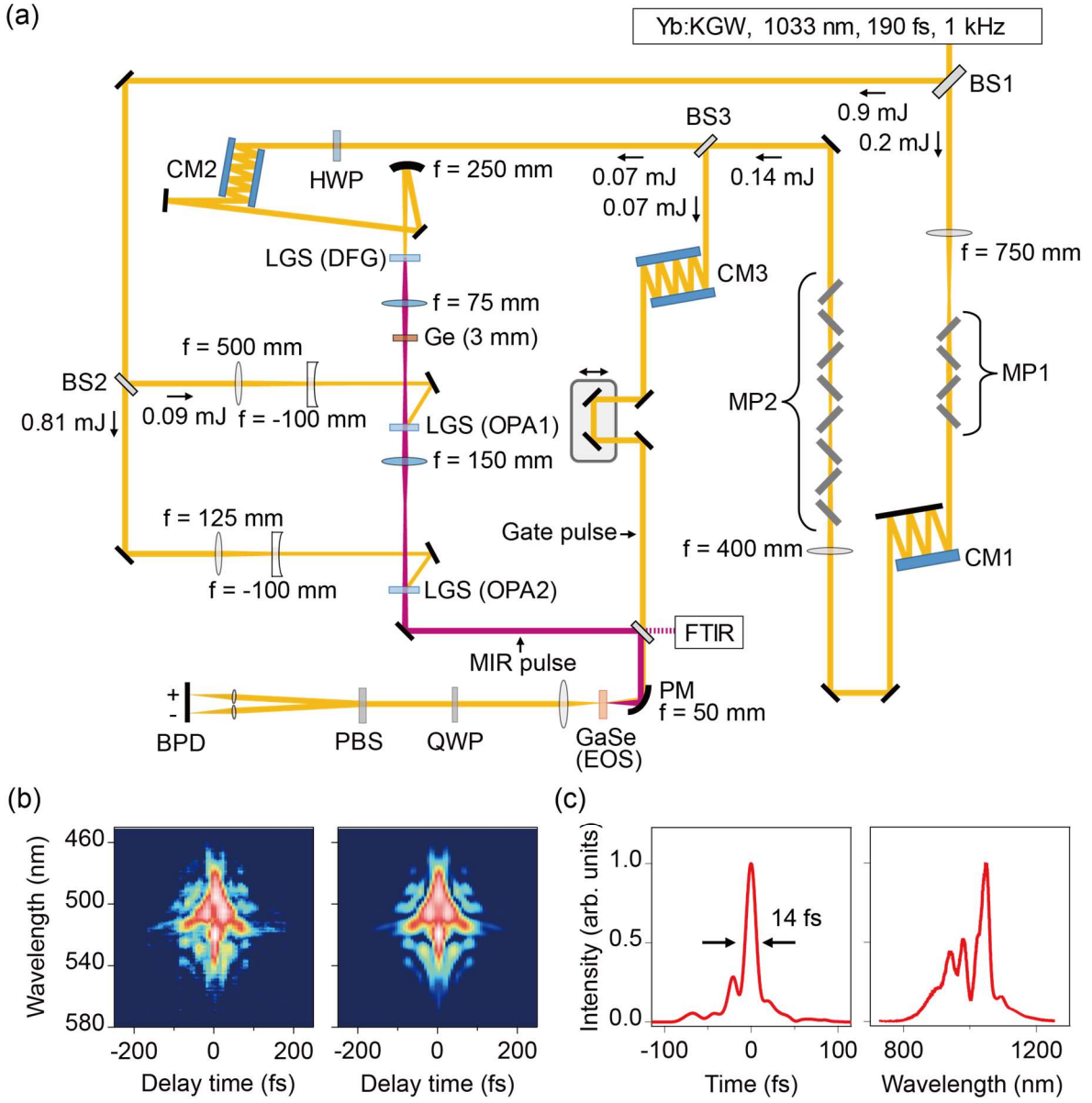
(a)

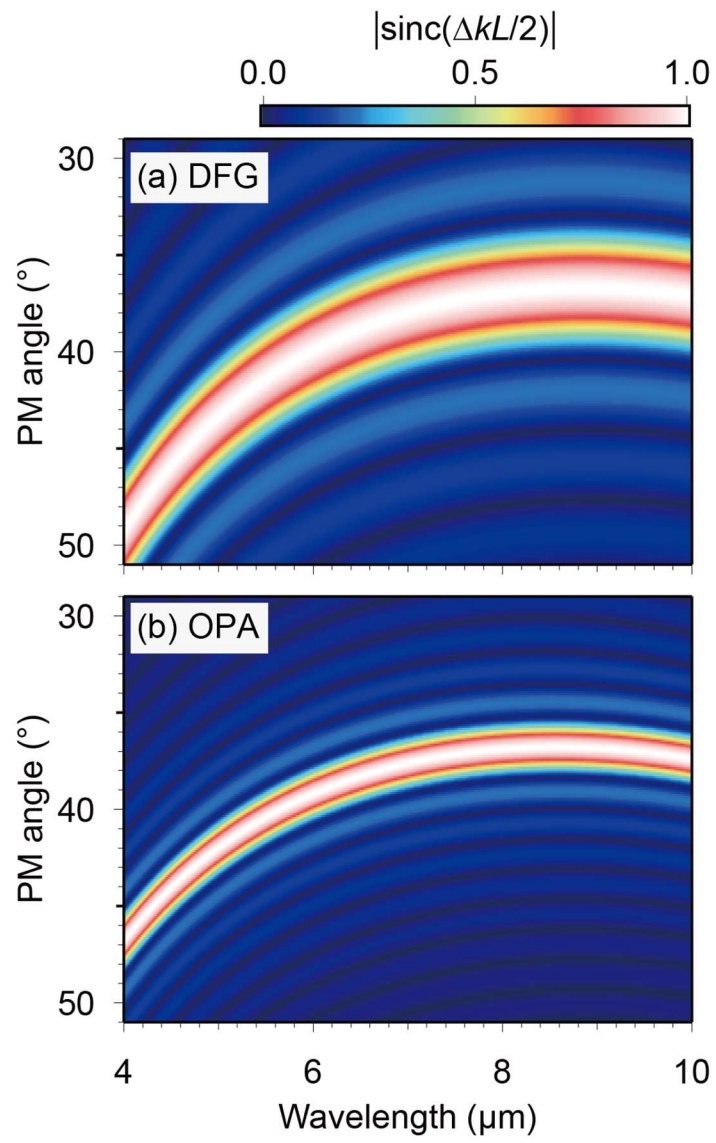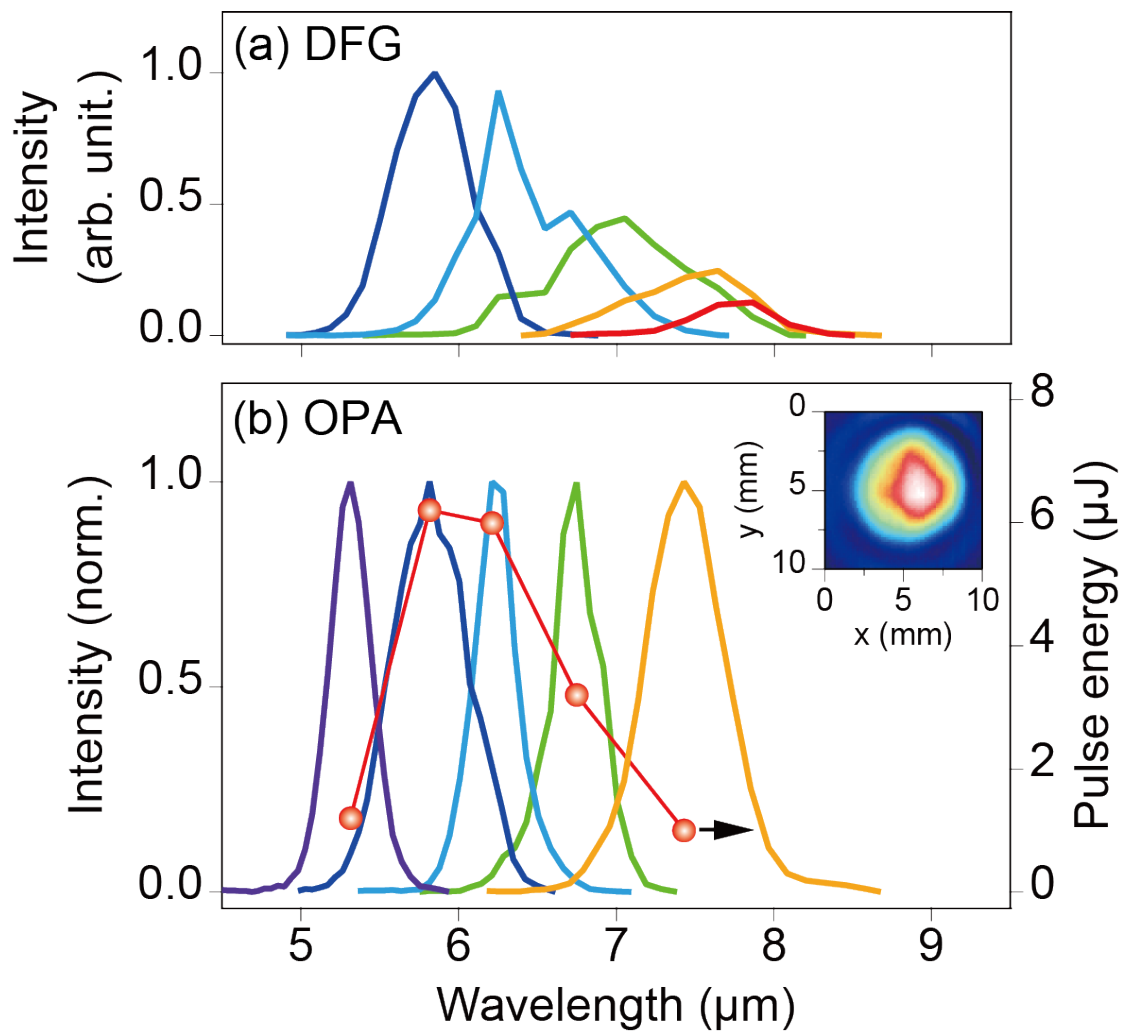Yb:KGW, 1033 nm, 190 fs, 1 kHz

BS1
0.9 mJ
0.2 mJ↓

BS3
0.07 mJ   0.14 mJ
0.07 mJ↓

CM2   HWP   f = 250 mm

f = 750 mm

LGS (DFG)

CM3

f = 75 mm
Ge (3 mm)

f = 500 mm

MP1

BS2   f = -100 mm
0.81 mJ↓   0.09 mJ

LGS (OPA1)

MP2

f = 150 mm

f = 125 mm

f = -100 mm   LGS (OPA2)

Gate pulse →

f = 400 mm

CM1

FTIR

MIR pulse

PM
f = 50 mm

+
−

BPD   PBS   QWP   GaSe
(EOS)

(b)

(c)

14 fs

Fig. 1.

11

Fig. 2.

Fig. 3.

Fig. 4.